1 **High-resolution prediction of organic matter concentration with**

2 **hyperspectral imaging on a sediment core**

3 Kévin Jacq[a,b], Yves Perrette[a], Bernard Fanget[a], Pierre Sabatier[a], Didier Coquin[b], Ruth

4 Martinez-Lamas[c,d], Maxime Debret[c], Fabien Arnaud[a]

5

6 a Univ. Grenoble Alpes, Univ. Savoie Mont Blanc, CNRS, EDYTEM, 73000 Chambéry, France

7 b Laboratoire d'Informatique, Systèmes, Traitement de l'Information et de la Connaissance

8 (LISTIC), Université Savoie Mont-Blanc, 74944 Annecy Le Vieux Cedex, France

9 c Laboratoire de Morphodynamique Continentale et Côtière, Université de Rouen, UMR

10 CNRS 6143, 76821 Mont-Saint-Aignan, France, Université de Caen, UMR CNRS 6143, 14000

11 Caen, France

12 d IFREMER, UR Géosciences Marines, Laboratoire Géophysique et Enregistrements

13 Sédimentaires, BP70, 29280 Plouzané, France

14

15 Corresponding Author:

16 Kévin Jacq

17 Environnements, Dynamiques et Territoires de la Montagne (EDYTEM)

18 Université Savoie Mont Blanc, Campus Scientifique,

19 73376 Le Bourget du Lac Cedex, France

20 kevin.jacq@univ-smb.fr

1   **Keywords**: Hyperspectral Imaging, Chemometrics, Near-Infrared Spectroscopy, High

2   Resolution Analysis, Organic Matter

3

4   **Abstract**

5

6   In the case of environmental samples, the use of a chemometrics-based prediction model is

7   highly challenging because of the difficulty in experimentally creating a well-ranged

8   reference sample set. In this study, we present a methodology using short wave infrared

9   hyperspectral imaging to create a partial least squares regression model on a cored

10   sediment sample. It was applied to a sediment core of the well-known Lake Bourget

11   (Western Alps, France) to develop and validate a model for downcore high resolution LOI550

12   measurements used as a proxy of the organic matter. In lake and marine sediment, the

13   organic matter content is widely used, for example, to reconstruct carbon flux variations

14   through time. Organic matter analysis through routine analysis methods is time- and

15   material-consuming, as well as not spatially resolved. A new instrument based on

16   hyperspectral imaging allows high spatial and spectral resolutions to be acquired all along a

17   sediment core. In this study, we obtain a model characterized by a 0.95 r prediction, with

18   0.77 wt% of model uncertainty based on 27 relevant wavelengths. The concentration map

19   shows the variation inside each laminae and flood deposit. LOI550 reference values obtained

20   with the loss on ignition are highly correlated to the inc/coh ratio used as a proxy of the

21   organic matter in X-ray fluorescence with a correlation coefficient of 0.81. This ratio is also

22   correlated with the averaged subsampled hyperspectral prediction with a r of 0.65.

23

1. Introduction

24

25

26 The organic matter is usually used for sediment studies. For example, it can be used to

27 estimate the carbon stocks over time. Among different methods, the organic matter can be

28 approximated through Loss of Ignition at 550°C (Heiri et al., 2001), which are a widely used

29 method in paleo-environmental studies. All these methods are time-consuming, relatively

30 expensive, destructive and have low spatial resolution (0.5-1 cm sampling).

31 Hyperspectral imaging is a method at the interface of spectroscopy and imaging. The

32 ability to predict the organic matter has been demonstrated based on visible (Vis, 400-800

33 nm) and near-infrared (NIR, 800-2500 nm) spectroscopy, known as Vis-NIR spectroscopy (Li

34 et al., 2015; Nawar and Mouazen, 2017; Van Exem et al., 2018; Viscarra Rossel and Behrens,

35 2010). Predictions are still efficient with only NIR spectroscopy (Clairotte et al., 2016; Leach

36 et al., 2008; Zornoza et al., 2008). Mid-infrared (MIR, 2500-25000 nm) spectroscopy also has

37 the same ability (Clairotte et al., 2016; Rosén et al., 2011; Vohland et al., 2014). X-ray

38 fluorescence (XRF) spectroscopy is also used as an indirect qualitative proxy of the organic

39 matter (Bajard et al., 2016; Chawchai et al., 2016; Croudace and Rothwell, 2015; Lintern et

40 al., 2016).

41 Chemometrics methods can be used to extract relevant information from spectral

42 bands by comparison with discrete sample measurements and can be used downstream to

43 predict the organic matter or other variables. Partial least squares regression (PLSR) has

44 probably been the most used method to extract organic matter information from spectra

45 (Clairotte et al., 2016; Dhawale et al., 2015; Nawar and Mouazen, 2017; Viscarra Rossel and

46 Behrens, 2010; Vohland et al., 2014). However, other methods can be used with their

3

47 specific conditions. For instance, the artificial neural network (ANN) and the support vector

48 machine (SVM) require a large dataset. A comparison of different chemometrics methods

49 show that advanced methods such as ANN, SVM, and Multivariate Adaptive Regression

50 Splines (MARS) can slightly improve the performance (Kuang et al., 2015; Li et al., 2015;

51 Viscarra Rossel and Behrens, 2010). Transferring a model between several samples can be

52 very interesting, and PLSR is better than ANN to model local variations, while they are quite

53 similar for global variations (Wijewardane et al., 2016). In order to improve model

54 performance and robustness, spectral variable selection is achieved to reduce the spectral

55 collinearity. As a side effect, this reduction makes chemical interpretation easier (Peng et al.,

56 2014; Viscarra Rossel and Behrens, 2010; Vohland et al., 2014). Furthermore, coupling

57 spectroscopic datasets have been shown to improve model performance (Clairotte et al.,

58 2016) by the increase of the spectral and thus chemical information.

59   Chemometrics methods have been widely used in the biochemistry and the

60 pharmacology domains. These methods are usually based on an experimentally built sample

61 set in which the target concentrations are known or spiked. A direct chemometrics approach

62 is promising to predict concentrations in environmental solids such as sediments, soils, and

63 biological tissues. The challenge is here to propose a procedure designed to build a robust

64 model based on a natural dataset only. Indeed, we can expect that the range and spread of

65 real target values of a learning dataset is less robust than a model generated with an

66 experimentally designed dataset.

67   The aim of this study is to propose a way to build a PLSR model with hyperspectral

68 data on a natural environmental sediment using the opportunity of its heterogeneity to

69 generate robust models without the constitution of an experimental set. We applied this

70   method to predict the organic matter content in a sediment core by the way of a PLSR

71   model. A sample from the Lake Bourget was used and analyzed with short-wave infrared

72   (SWIR, 900-2500 nm) hyperspectral imaging. The loss on ignition (LOI) was the reference

73   method for the organic matter values. LOI is predicted from a hyperspectral image and a

74   variable selection applied to increase the robustness of the model. Predictions were

75   validated with LOI550 measurements and compared with the inc/coh ratio calculated with

76   XRF as a qualitative proxy of the organic matter. Finally, the pixel prediction validity with the

77   scale law (micrometer and millimeter) is discussed.

78

79   **2.   Materials and methods**

80

81   2.1.   Site descriptions

82

83   Lake Bourget (231.5 masl, 18 km long, and 2.8 km wide) is a hard-water lake at the

84   northwestern edge of the French Alps (figure 1). The lake was formed between the Pre-

85   Alpine and Jura Mountain ranges within the Molasse Basin by the retreat of Wurmian

86   glaciers. Two small rivers (Leysse and Sierroz) usually flow into Lake Bourget, which then

87   flows into the Rhone River by the Saviere Channel. However, during flooding of the Rhone

88   River, the water-current of this channel is reversed, and river water flows into Lake Bourget.

89   In the northern deep basin, flood deposits from the Rhone contribute to a variable

90   sediment fraction. During such flood events, the Lake Bourget catchment area is 4,600 km^2,

91   including tributaries draining part of the Jura Mountains and the Inner Alps. Otherwise,

92   excluding the Rhone, it is 580 km^2. Over the last 10,000 years, the river-borne silicate

93   fraction has ranged between 10 and 40% of the bulk sediment, with the remaining amount

94   composed of carbonate depending on past climate conditions (Arnaud et al., 2012, 2005;

95   Debret et al., 2010; Giguet-Covex et al., 2010; Jenny et al., 2014).

96   In 2009, sediment (LDB09-P101, length = 54 cm, width = 9 cm) was cored in the

97   northern basin of Lake Bourget (N45 45.334, E5 51.332, 145 m water depth) in the frame of

98   the IPER-RETRO program (ANR-08-VUL 005, (Perga et al., 2015)). This core was selected for

99   this study because it contains both seasonally paced bioinduced millimeter lamina as well as

100   interbedded deposits brought by Rhone River flood events.

101

102   2.2.   Sample preparation and LOI550 measurement

103

104   The core was sampled every ca. 2 cm in 5 mm slices cautiously avoiding the mixing of

105   different sediment facies (i.e., lamina and flood deposits for example). However, in this 5

106   mm, there can be several lamina which are around 2 mm thick. Discrete samples were dried

107   at 60 °C for 72 h then crushed (Basma et al., 1994).

108   The LOI was measured following the methodology detailed in (Heiri et al., 2001). Briefly, the

109   protocol is as follows: (1) heat to 550 °C over 4 h to estimate the organic content and (2)

110   heat to 950 °C over 2 h to estimate the mineral carbon content. At each step, the sample

111   was weighed to calculate the loss of weight (wt%) with equations (1) and (2).

112

$$LOI550 \ (wt\%) = \frac{m_0 - m_1}{m_0} * 100 \qquad (1)$$

$$LOI950 \ (wt\%) = \frac{(m_1 - m_2)}{m_0} * 100 \qquad (2)$$

113

114   where m_0 is the initial weight of dried sediment, m_1 is the weight after the first step,

115   and m_2 is the weight at the end.

116   The uncertainty of this method is 0.14 wt% ($\alpha = 0.05$, $n = 63$) for LOI550 values and

117   0.04 wt% ($\alpha = 0.05$, $n = 63$) for LOI950 values. It was estimated with 7 samples and 9

118   replicates each from several cores.

119

120   2.3.   SWIR hyperspectral imaging acquisition

121

122   Hyperspectral imaging consists of acquiring an image with high spatial resolution, in which

123   each pixel contains spectral information with a continuous spectral resolution.

124   The core was analyzed in less than 15 minutes with the SWIR hyperspectral camera

125   (Specim Ltd., Finland) with the lens OLES22,5 at the M2C lab, University of Normandie-

126   Rouen. It covers the SWIR range between 968 nm and 2574 nm with a reflectance spectral

127   resolution of 12 nm (144 wavelengths) and a spatial theoretical resolution of 200 µm in both

128   directions all along the core. The spectral unit is reflectance by 10,000 (R x 10,000).

129   The protocol followed to acquire the hyperspectral image is detailed in (Butz et al.,

130   2015). The core was cleaned before acquisition. Then, the camera was calibrated with a

131   spectralon reference (white), and the shutter was closed (black) for determining the spectral

132   dimensions. Spatial calibration was achieved by the way of imaging a known object for its

133   shape (squared pixels) and color (intensity). Deviation was checked at the end of the

134   acquisition in the same manner, and no deviation was observed.

135

136   2.4.   X-ray fluorescence spectroscopy

137

138   The relative contents of major elements were analyzed by X-ray fluorescence (XRF) at a 200

139   μm resolution on the surface of the sediment core with an ITRAX XRF Core Scanner (Cox

140   Analytical Systems) at the CEREGE laboratory in 2010. The split core surface was first

141   covered with a 4-μm-thick Ultralene film to avoid contamination and desiccation of the

142   sediment. The X-ray beam was generated with a molybdenum tube at 35 kV and 30 mA, with

143   a runtime of 15 s. Compton (incoherent) and Rayleigh (coherent) scattering data were

144   extracted from it, and the inc/coh ratio was calculated. It has been used in many studies as a

145   qualitative proxy of organic matter (Bajard et al., 2016; Chawchai et al., 2016; Croudace and

146   Rothwell, 2015; Lintern et al., 2016).

147

148   2.5.   Data analysis

149

150   Data acquisition was performed using Specim hardware ENVI 4.8. The data was then

151   converted, processed and analyzed with MATLAB (R2017a, MathWorks). Several free and

152   open MATLAB toolboxes were used and are detailed afterwards.

153   A key point to predict the LOI550 from hyperspectral imaging is the coupling of the

154   volume of the sample at 5 mm resolution with surface pixels of approximately 0.2 mm. The

155   proposed method is composed of four main steps. (1) A bootstrapping selection in the

156   hyperspectral spectra of the LOI sampling area was performed to construct several datasets.

157   (2) Then, PLSR was used to model LOI550 thanks to these spectra and the discrete LOI550

158   measurements for all the datasets. (3) The 10 optimal models were retained based on their

159 performances. (4) Wavelengths highly correlated with LOI550 were identified with variable

160 selection on the retained models in (3). A final reduced model was estimate with these

161 wavelengths. The complete workflow followed in this study is presented in Figure 2.

162

163   2.5.1. Spectral preprocessing

164

165 Spectral bands between 968-1127 nm (15 wavelengths) and 2418-2574 nm (15 wavelengths)

166 were excluded from the processing because of their very low signal-to-noise ratio. In fact,

167 noise is known to artificially increase the prediction of a chemometrics model (Tetko et al.,

168 1995). 39 wavelengths of H_2O absorption bands (between 1094 and 1176 nm, 1339 and

169 1465 nm, and 1773 and 2005 nm) were removed as proposed by (Gomez et al., 2015).

170 Consequently, 75/144 wavelengths were retained (figure 3).

171   In order to produce a robust model, some data in the spectra and LOI550 values have

172 been removed based on two standard deviations of the Mahalanobis distance in a principal

173 component analysis space (Mark and Tunnell, 1985). These data were due to spectral

174 artifacts (specular reflection, not enough signal, too noisy) or aberrant values. Pixels that

175 correspond to high surface variations (gap areas for example) were removed by setting a

176 lower limit for the standard deviation of a spectrum. This threshold must be set for each

177 image and based on the spectrum regions without noisy bands. For Lake Bourget images, a

178 standard deviation limit is set at 250 R x 10,000 (reflectance per 10,000).

179   Several standard spectral preprocessing (detrend, standard normal variate (SNV),

180 Savitzky-Golay derivatives) were tested to correct spectra from the scattering effect and/or

181 to normalize spectra (Vidal and Amigo, 2012). Finally, in order to optimize the prediction

182   model, the data were preprocessed by the way of an autoscaling by mean-centering and

183   standardizing each wavelength (Z-score).

184

185   2.5.2. Spectral sub-sampling

186

187   Our goal is to build a regression model between a set of 20 data of LOI and a set of 20

188   regions of thousands of pixels on the image which correspond to the sampling area.

189   Different techniques could be used to generate a representative value of the spectrum used

190   for regression with LOI data, (mean, bootstrap, min or max, mode or median spectrum). The

191   limit of a mean spectrum for each sampling area leads to smooth spectral variabilities;

192   resulting model were not relevant. We applied a bootstrapping procedure rather than a

193   mean spectrum assuming that LOI could be better explained by a specific spectrum of the

194   region of interest than by the mean spectrum of this region. Bootstrapping was used to

195   randomly select 100 spectra in each sampling area to generate 100 datasets of 20 spectra.

196

197   2.5.3. Partial least squares regression

198

199   PLSR was used to establish a relationship between the LOI550 values and SWIR

200   hyperspectral imaging. This method is based on the extraction of orthogonal predictors (also

201   called latent variables, LV) corresponding to the maximum variability in the spectral bands

202   used as predictors linked to one or several predicted variable(s) (Wold et al., 1984).

203   Each of the 100 bootstrapped datasets was divided in a calibration set (13 data) and a

204   validation set (the 7 unused data). For each of the 100 bootstrapped datasets, a PLSR model

205   is generated based on the calibration set, and then applied to the validation set in order to

206   assess the performances of the prediction.

207   The optimal number of latent variables was estimated by the use of the Durbin

208   Watson test (Durbin and Watson, 1950) which is similar to a signal-to-noise ratio and was

209   used to improve the robustness of the model.

210   Performances of the prediction model were estimated using the coefficient of

211   correlation, r, and the uncertainty of both data sets (calibration and validation sets). They

212   are calculated by equations (3) and (4).

$$r = \sqrt{1 - \frac{\sum_{i=1}^{n}(y_i - \hat{y}_i)^2}{\sum_{i=1}^{n}(y_i - \overline{y}_i)^2}} \qquad (3)$$

$$Model\ uncertainty = 2 \times \sqrt{\frac{\sum_{i=1}^{n}(\hat{y}_i - y_i)^2}{n}} \qquad (4)$$

213   where y_i is a LOI550 reference value, $\hat{y}_i$ is a LOI550 predicted value, $\overline{y}_i$ is the mean

214   LOI550 reference value, and n is the number of values.

215

216

217   2.5.4. Variable selection

218

219   Variable selection algorithms were used to decrease the redundancy between neighboring

220   wavelengths and remove non-informative ones to make the models more robust and easier

221   to interpret chemically. The algorithms that were used can be found in MathWorks and are

222   detailed in (Leardi and Lupiáñez, 1998; Li et al., 2014). The genetic algorithm was the

223   method that gives the optimal model performance, as it aims is to solve an optimization

224 problem by finding the lowest number of wavelengths to have the optimal prediction

225 performance. It is inspired by natural selection, where wavelengths that are highly

226 correlated to the LOI550 are first selected and then the optimal combination is chosen.

227 The GA-PLSR of the 10 best performing bootstrapping models were used to increase the

228 certainty for the selected wavelengths. Then, the wavelengths are ranked by their number of

229 occurrences. PLSR models are calculated by increasing the number of ranked selected

230 wavelengths. Finally, a model is chosen with the optimal r and model uncertainty. At last, a

231 geochemical map is estimated by the prediction of all the hyperspectral pixels to observe the

232 distribution down and across the core. Once an optimal model is created, it can be used

233 theoretically without other sampling on other cores sampled in the similar sedimentation

234 environment.

235

236 **3. Results**

237

238 3.1. Lithology and OM content

239

240 The Lake Bourget sediment core presents three main units, which were described in detail in

241 (Giguet-Covex et al., 2010). The uppermost one, between 0 cm and 18 cm, presents

242 millimeter-thick biochemical varve and corresponds to anoxic conditions at the lake-

243 sediment interface, with LOI550 values greater than 6 wt% (Giguet-Covex et al., 2010; Jenny,

244 2013). The second unit, between 18 cm and 26 cm, presents disturbed varve and LOI550

245 values that are stable at 6 wt%. In the lowermost unit, between 26 cm and 54 cm, there are

246 fuzzy laminated structures, and the LOI550 values are quite stable at 5 wt%. Flood-triggered

247 deposits (Jenny et al., 2014) are also present in the two first units, with a major one between

248 13.5 cm and 14.5 cm. Twenty measurements of the LOI were performed with a range

249 between 4.97 wt% and 8.60 wt% and a mean value of 6.41 wt% along with a standard

250 deviation of 1.37 wt%. LOI550 variations according to the depth can be seen in figure 4.d.

251

252 3.2. Organic matter predictive models

253

254 Four PLSR models are presented in table 1 to illustrate the importance of removing water

255 bands and wavelength selection.

256 Having a high number of LVs can increase the r of calibration but decrease the model

257 robustness because more LVs increase the calibration noise, which is not present in the

258 validation set. This is shown between models with and without water bands (table 1 blue

259 and green). When the number of LVs is higher, the calibration r is too, but the validation r is

260 lower.

261 Wavelength selection leads to increase the performance of the prediction model.

262 This is visible with a number of latent variables (LV) that is smaller (6-8) and an uncertainty

263 that decreases when less wavelengths are used.

264 Finally, the best compromise was found with a model with 27 wavelengths, validated

265 with 6 latent variables, and a prediction r of 0.95 ($p < 0.05$). A model uncertainty of 0.77

266 wt% ($\alpha = 0.05$, $n = 20$) for LOI550 prediction by hyperspectral imaging was found, whereas it

267 is 0.14 wt% ($\alpha = 0.05$, $n = 20$) for the LOI550 analysis. This is in agreement with PLSR models

268 developed with spectroscopic devices in the literature (Clairotte et al., 2016; Leach et al.,

269 2008; Li et al., 2015). This uncertainty is quite important because of the low number of

270 LOI550 values and their low dispersion. We expect that a greater and spreader set of LOI

271 values should lead to a more accurate PLSR model.

272

273   3.3.   Wavelength correlation with organic matter

274

275 Variable selection algorithms are dependent on the spectral preprocessing (Peng et al.,

276 2014). First models with O-H bands show that they were selected as relevant, whereas some

277 organic bands were missing. These models, however, were less robust in terms of prediction.

278 These results could depend on O-H water bands that disturb the model. Removing O-H

279 wavelengths can increase the performance and robustness if other bands can add relevant

280 information to replace the missing information of organic matter O-H bands.

281   The genetic algorithm allows the number of wavelengths to be reduced to 27 (figure

282 3). They can be divided into three main classes, organic, carbonate and clay bands according

283 to (Peng et al., 2014; Viscarra Rossel and Behrens, 2010). Organic bands correspond to C-H

284 bonds (1205, 1217, 1622, 1735, 1746, 1757, 2250, 2261, 2272, 2306, 2317, and 2328 nm), C-

285 O bonds (2127 and 2138 nm), and N-H bonds (2093, 2105, and 2116 nm). Bands associated

286 with C=O bonds (1487 and 1510 nm) corresponds to organic or carbonate bands, and these

287 may discriminate the lamina type (dark or light). For clay bands, 5 bands were selected

288 (2149, 2160, 2183, 2228, and 2239 nm). The three other bands are not directly associated

289 with chemical bonds (1273, 1555, and 1566 nm). Some bands are spectrally close (for

290 example, 1205-1217 nm and 1746-1757 nm), which could reveal some band shape changes

291 due to organic mineral interaction.

292

293   3.4.   Range, prediction and confidence intervals

294

295   The PLSR model was made with LOI550 measurements that have a range of 4.97 wt% to 8.60

296   wt%. We assume that LOI550 model intercept at the origin (there is no organic matter

297   spectroscopic signal when there is no organic matter in the sediment). Then we consider

298   that we can predict LOI550 in the range 0 wt% to 8.60 wt%. 93 % of the data are included in

299   it and have a minimal prediction error of 2.25 wt% ($\alpha = 0.05$) in the center of the calibration

300   (6.26 wt%).

301   Prediction and confidence intervals were calculated thanks to the complete dataset

302   (figure 5.c). The prediction error map (figure 5.b) shows side effects (right and left), which

303   can be due to surface variation or illumination. This observation is also visible in the

304   concentration map. Obviously, areas with high surface variations (gap, fissures) will not be

305   used in the LOI550 profile, and their prediction errors are more important than other

306   predicted values at the same depth. Figure 5.e shows that the prediction error is high in the

307   middle of light lamina (near 2.90 wt%), whereas it is low for the dark lamina (near 2.30 wt%).

308   Predictions of these light lamina concentrations have a range between 9-12 wt% (figure 5.d).

309   These predictions, out of the calibration range, must be interpreted cautiously.

310

311   3.5.   Prediction distribution

312

313   The LOI550 concentration map in figure 4.c shows the three lithology units. A horizontal

314   merging is used to estimate a time series of LOI550 (figure 4.e) prediction to be compared

315   with LOI550 reference values (figure 4.d). The first unit presents LOI550 prediction values

316 that oscillate with a maximum near 11 wt% and a minimum of 4 wt%, and the global trend is

317 a decrease from 11 wt% to 6 wt%, which is similar to the reference values. The second unit is

318 characterized by a lower variation between 5-7 wt% and a steady trend at approximately 6

319 wt%. The last unit is quite homogeneous at 5 wt%. Floods can be characterized with a rapid

320 decrease in the prediction value, for example, the one between 13.5 and 14.5 cm.

321 　　　　Focusing on unit 1, the variations of the average LOI550 predicted values (figure 6.a,

322 blue curve) appear to closely match the varve laminations, with high values for light lamina

323 and low values for black lamina. This is also in agreement with the LOI550 reference values

324 (green line) by averaging a 5 mm thickness. In the LOI550 concentration map (figure 6.b), the

325 sequence of varve is observable along the core with 200 µm resolution. Even if values are

326 out of the range, a qualitative study can be made. Variations inside light lamina show that

327 the middle has a higher concentration than the edges, and for dark lamina, an opposite

328 trend exists, with the lowest values in the middle. There can be mixing between lamina

329 inside the sediment or inside the spectra. Additionally, it is heterogeneous across lamina

330 with LOI550 variations. In a flood, the average LOI550 predicted values (figure 6.c) present

331 an upward decreasing trend from 5 wt% to 6.5 wt%. The LOI550 concentration map (figure

332 6.d) shows that values vary a lot, approximately 3 wt% across the core.

333

334 **4. Discussion**

335

336 　　4.1.　　　Comparison of LOI550 with the inc/coh ratio by XRF

337

16

338   In order to discuss this prediction, we compare this prediction with another proxy of organic

339   matter which can be measured at a similar spatial resolution. The incoherent to coherent

340   ratio was calculated with an XRF core scanner on this core. This ratio is used as an indirect

341   qualitative proxy of the organic matter, whereas the LOI550 is quantitative. To ensure the

342   pertinency of the comparison of PLSR model and inc/coh proxy, we compare first with

343   LOI550 with this proxy for this sample.

344   This ratio has been subsampled, the 25 pixels corresponding to 5 mm of LOI550 were

345   averaged. LOI550 measurements and the inc/coh are correlated (r = 0.81; $p < 0.05$) and can

346   thus be compared. Figure 4.d,e show that differences are mainly in unit 2 with inc/coh

347   values similar to unit 1, whereas LOI550 measurements between these two units are

348   decreasing. This could be due either to the surface state (oxidation) or to the difference

349   between a surface (inc/coh) and a volume (LOI550) measurement.

350   The hyperspectral quantitative prediction can also be compared with the inc/coh

351   ratio when resampled at the same resolution. Figure 4.f shows the ratio variations along the

352   core, and the three units are characterized with high, medium, and low oscillations in the

353   hyperspectral prediction as well as variation in the flood deposit. The correlation coefficient

354   between the LOI550 prediction and inc/coh is 0.65 ($p < 0.05$). With the high-resolution

355   image on varved lamina (figure 6.a, c), it is easier to show and compare both variations. The

356   LOI550 quantitative prediction and inc/coh qualitative ratio are in agreement for varve

357   lamina and flood deposits. When the varve are not parallel or mixed, XRF cannot detect

358   them, whereas hyperspectral imaging can, and that can be seen at a 4 cm depth. Between

359   depths of 3.2 cm and 3.6 cm, values of inc/coh and predicted LOI550 are steady because of

360   the presence of irregularly shaped varve. For hyperspectral imaging, it is possible to see

17

361   them on the concentration map, and with image processing, it will be possible to adjust the

362   varve sequence. For the flood (figure 6.c), the inc/coh ratio increases faster down the core

363   than the hyperspectral prediction, which may indicate that one of the two methods is biased

364   by grain size variations.

365

366   4.2.   Micrometric surface prediction and volume analysis

367

368   The analysis of the LOI550 *vs* inc/coh leads to suspect a difference between surface *vs*

369   volume measurement. This volume-surface correlation is noted $r_{V/S}$. LOI550 measurements

370   and the average predicted values are correlated with a $r_{V/S}$ of 0.73 ($p < 0.05$) and a root

371   mean square error (RMSE) of 1.72 wt%.

372   Some points between depths of 6 cm and 12 cm are affected by a surface variations

373   such as the gap on the top right of the core (figure 4.a, c), and without this area, the

374   correlation $r_{V/S}$ increased to 0.81 ($p < 0.05$). This induces a loss of spectral intensity and thus

375   weaker LOI550 prediction values. Cores need to have as large as possible of a plane surface

376   to have a correct prediction.

377   The $r_{V/S}$ is weaker than that of the model due mainly to chemical properties. The

378   surface state can be the main explanation, as the oxidation of some chemical compounds

379   can induce intensity variations on the selected bands in some pixels. That is why the core

380   needs to be cleaned before beginning, and the acquisition needs to be fast for no

381   reappearance of surface states between the first and the last spectra. The other differences

382   can mean that the surface and volume sediment analysis don't evaluate the same property

383   for the organic matter content.

18

384

385   4.3.   Proposed methodology

386

387 The proposed methodology seems to be relevant with the validation of PLSR models by XRF

388 comparison and by the characteristics of the chemical bonds selected with the variable

389 selection algorithm. However, based on the concentration map and selected spectral bands,

390 we can wonder if a unique PLSR model is the optimal method in a sediment characterized by

391 three different mineralogical patterns: the two types of lamina (light and dark) and the

392 homogeneous part. If PLSR models were created for each of these three patterns

393 independently, prediction could be more accurate with different selected wavelengths. With

394 our LOI measurements, it is not possible to estimate a model by the type of lamina because

395 the sampling resolution of an operator does not allow the ability to distinguish between

396 them. Improvement of such a model could occur by the way of a higher sampling resolution

397 that is closer to the lithology of the sediment core.

398

399   4.4.   Outlook for PLSR application on sediment cores and other

400   environmental matrices

401

402 Quantitatively predicting proxies at high resolution along and across the core in less than an

403 hour, from the acquisition to the prediction, is very effective and is not done by any other

404 methods at this time. This is an important advance for the study of sediment cores to infer

405 the paleo-environment and paleo-climate. The high spatial resolution allows us to look inside

406 the laminae, and the spectral dimensions allow chemical variations to be studied with

407   further work to identify the patterns of organic matter. The high-resolution approach is

408   relevant in some type of sedimentary environments where there are successive deposits as

409   the lamina or the varve and even in some homogenous sediment. In the case of a very

410   homogeneous sediment such as those subject to bioturbation or redistribution, the high

411   resolution loses some interests, but the detection of specific compounds may still keep an

412   interest for a global characterization (without chronology).

413   The use of other proxies may help to improve the quality of the predictions. With this

414   application on the Lake Bourget core, grain size effects seem to skew the LOI550 modeling.

415   Predicting several proxies at the same time can make the model more robust. For example, if

416   the grain size has a real effect on the LOI550 prediction, creating a unique model could

417   increase the robustness. Furthermore, the spatial and the spectral dimensions of the

418   hyperspectral images may be combined in the data processing to improve our understanding

419   of the sediment records. For instance, thanks to lamina, chemical, physical and biological

420   variations could be estimated at the seasonal scale. In the Lake Bourget core, organic carbon

421   fluxes could be estimated for each type of laminae (dark or light) and compared in eutrophic

422   and non-eutrophic parts of the core (Jenny, 2013).

423   Creating a universal model that can be applied to several sedimentation sites (lake,

424   marine, etc.) and types (eutrophic, detrital, etc.) needs standardized parameters. Obviously,

425   the hyperspectral acquisition is a critical step that need to follow a strict protocol (Butz et al.,

426   2015). Even if a model seems to be applied to a core which was not used on the model

427   generation, some few chemical verifications may be achieved in order to avoid unexpected

428   bias. As a first step, the model could be theoretically transferred on samples cored in similar

429   sedimentary environments to keep the same type of matrix effects.

430   Obviously, with all these considerations, this methodology can be transferred to

431   other natural heterogeneous samples, for example speleothems, soils, ice cores, and trees,

432   to infer the paleo-environment, paleo-climate, soil health, and pollution.

433

434   **5. Conclusion**

435

436   Hyperspectral imaging is a high resolution (200 µm), nondestructive and fast analysis

437   method (15 minutes). Coupling hyperspectral imaging and partial least squares regression

438   shows great possibilities for the creation of quantitative predictive models and the

439   prediction for any kind of natural sample at high resolution. In this study, a methodology was

440   proposed to estimate a robust PLSR model using the heterogeneity of the sample without

441   the constitution of a specific calibrated concentration range.

442   It was applied to LOI550 prediction and it was validated with LOI550 measurements

443   with selected near-infrared wavelengths that correspond to relevant chemical bonds. It was

444   also successfully compared with the inc/coh XRF qualitative ratio used as a proxy of the

445   organic matter. Therefore, this methodology seems to be relevant and allows for the organic

446   matter content to be quantitatively inferred at high resolution along and across the core.

447   This proxy for laminated or varve sediment could be precise at the seasonal scale with the

448   200 µm pixel size.

449   This methodology must be tested on other cores or heterogeneous samples to verify

450   its relevance. The "universality" of the model generated from this dataset, should be applied

451   on different lake systems in order to test the ability to predict organic matter in other

452   environments and to set the limitations of this. It may be used on other proxies that are

453   characteristic in the basin catchment. Predicting several proxies at the same time may also

454   be studied to create a robust model that is not disturbed by some chemical or physical

455   variabilities. The proposed methodology applied to sediment cores has great possibilities to

456   more precisely infer the paleo-climate and paleo-environment that are recorded in the core

457   inside each sediment structure.

458

459   **Acknowledgements**

460

465 **References**

466

467 Arnaud, F., Revel, M., Chapron, E., Desmet, M., Tribovillard, N., 2005. 7200 years of Rhône

468   river flooding activity in Lake Le Bourget, France: a high-resolution sediment record of

469   NW Alps hydrology. Holocene 15, 420–428.

470   https://doi.org/10.1191/0959683605hl801rp>

471 Arnaud, F., Révillon, S., Debret, M., Revel, M., Chapron, E., Jacob, J., Giguet-Covex, C.,

472   Poulenard, J., Magny, M., 2012. Lake Bourget regional erosion patterns reconstruction

473   reveals Holocene NW European Alps soil evolution and paleohydrology. Quat. Sci. Rev.

474   51, 81–92. https://doi.org/10.1016/j.quascirev.2012.07.025

475 Bajard, M., Sabatier, P., David, F., Develle, A.-L., Reyss, J.-L., Fanget, B., Malet, E., Arnaud, D.,

476   Augustin, L., Crouzet, C., Poulenard, J., Arnaud, F., 2016. Erosion record in Lake La Thuile

477   sediments (Prealps, France): Evidence of montane landscape dynamics throughout the

478   Holocene. The Holocene 26, 350–364. https://doi.org/10.1177/0959683615609750

479 Basma, A.A., Al-Homoud, A.S., Al-Tabari, E.Y., 1994. Effects of methods of drying on the

480   engineering behavior of clays. Appl. Clay Sci. 9, 151–164. https://doi.org/10.1016/0169-

481   1317(94)90017-5

482 Butz, C., Grosjean, M., Fischer, D., Wunderle, S., Tylmann, W., Rein, B., 2015. Hyperspectral

483   imaging spectroscopy: a promising method for the biogeochemical analysis of lake

484   sediments. J. Appl. Remote Sens. 9, 1–20. https://doi.org/10.1117/1.JRS.9.096031

485 Chawchai, S., Kylander, M.E., Chabangborn, A., Löwemark, L., Wohlfarth, B., 2016. Testing

486   commonly used X-ray fluorescence core scanning-based proxies for organic-rich lake

487   sediments and peat. Boreas 45, 180–189. https://doi.org/10.1111/bor.12145

488   Clairotte, M., Grinand, C., Kouakoua, E., Thébault, A., Saby, N.P.A., Bernoux, M., Barthès,

489   B.G., 2016. National calibration of soil organic carbon concentration using diffuse

490   infrared reflectance spectroscopy. Geoderma 276, 41–52.

491   https://doi.org/10.1016/j.geoderma.2016.04.021

492   Croudace, I.W., Rothwell, R.G., 2015. Micro-XRF studies of sediment cores : applications of a

493   non-destructive tool for the environmental sciences. https://doi.org/10.1007/978-94-

494   017-9849-5

495   Debret, M., Chapron, E., Desmet, M., Rolland-Revel, M., Magand, O., Trentesaux, A., Bout-

496   Roumazeille, V., Nomade, J., Arnaud, F., 2010. North western Alps Holocene

497   paleohydrology recorded by flooding activity in Lake Le Bourget, France. Quat. Sci. Rev.

498   29, 2185–2200. https://doi.org/10.1016/J.QUASCIREV.2010.05.016

499   Dhawale, N.M., Adamchuk, V., Prasher, S.O., Viscarra Rossel, R.A., Ismail, A.A., Kaur, J., 2015.

500   Proximal soil sensing of soil texture and organic matter with a prototype portable mid-

501   infrared spectrometer. Eur. J. Soil Sci. 66, 661–669. https://doi.org/10.1111/ejss.12265

502   Durbin, J., Watson, G.S., 1950. Testing for Serial Correlation in Least Squares Regression: I.

503   Biometrika 37, 409–428. https://doi.org/10.2307/2332391

504   Giguet-Covex, C., Arnaud, F., Poulenard, J., Enters, D., Reyss, J.-L., Millet, L., Lazzaroto, J.,

505   Vidal, O., 2010. Sedimentological and geochemical records of past trophic state and

506   hypolimnetic anoxia in large, hard-water Lake Bourget, French Alps. J. Paleolimnol. 43,

507   171–190. https://doi.org/10.1007/s10933-009-9324-9

508   Gomez, C., Drost, A.P.A., Roger, J.M., 2015. Analysis of the uncertainties affecting predictions

509   of clay contents from VNIR/SWIR hyperspectral data. Remote Sens. Environ. 156, 58–

510   70. https://doi.org/10.1016/j.rse.2014.09.032

511   Heiri, O., Lotter, A.F., Lemcke, G., 2001. Loss on ignition as a method for estimating organic

512   and carbonate content in sediments: reproducibility and comparability of results. J.

513   Paleolimnol. 25, 101–110. https://doi.org/10.1023/A:1008119611481

514   Jenny, J.-P., 2013. Réponses des grands lacs périalpins aux pressions anthropiques et

515   climatiques récentes : reconstitutions spatio-temporelles à partir d'archives

516   sédimentaires. HAL. Université Grenoble Alpes.

517   Jenny, J.-P., Wilhelm, B., Arnaud, F., Sabatier, P., Giguet Covex, C., Mélo, A., Fanget, B.,

518   Malet, E., Ployon, E., Perga, M.E., 2014. A 4D sedimentological approach to

519   reconstructing the flood frequency and intensity of the Rhône River (Lake Bourget, NW

520   European Alps). J. Paleolimnol. 51, 469–483. https://doi.org/10.1007/s10933-014-9768-

521   4

522   Kuang, B., Tekin, Y., Mouazen, A.M., 2015. Comparison between artificial neural network and

523   partial least squares for on-line visible and near infrared spectroscopy measurement of

524   soil organic carbon, pH and clay content. Soil Tillage Res. 146, 243–252.

525   https://doi.org/10.1016/j.still.2014.11.002

526   Leach, C.J., Wagner, T., Jones, M., Juggins, S., Stevenson, A.C., 2008. Rapid determination of

527   total organic carbon concentration in marine sediments using Fourier transform near-

528   infrared spectroscopy (FT-NIRS). Org. Geochem. 39, 910–914.

529   https://doi.org/10.1016/j.orggeochem.2008.04.012

530   Leardi, R., Lupiáñez, A., 1998. Genetic algorithms applied to feature selection in PLS

531   regression: how and when to use them. Chemom. Intell. Lab. Syst. 41, 195–207.

532   https://doi.org/10.1016/S0169-7439(98)00051-3

533   Li, H., Xu, Q., Liang, Y., 2014. libPLS: An Integrated Library for Partial Least Squares

534   Regression and Discriminant Analysis. PeerJ Prepr.

535   https://doi.org/10.7287/peerj.preprints.190v1

536 Li, S., Shi, Z., Chen, S., Ji, W., Zhou, L., Yu, W., Webster, R., 2015. In Situ Measurements of

537   Organic Carbon in Soil Profiles Using vis-NIR Spectroscopy on the Qinghai-Tibet Plateau.

538   Environ. Sci. Technol. 49, 4980–4987. https://doi.org/10.1021/es504272x

539 Lintern, A., Leahy, P.J., Zawadzki, A., Gadd, P., Heijnis, H., Jacobsen, G., Connor, S., Deletic,

540   A., McCarthy, D.T., 2016. Sediment cores as archives of historical changes in floodplain

541   lake hydrology. Sci. Total Environ. 544, 1008–1019.

542   https://doi.org/10.1016/j.scitotenv.2015.11.153

543 Mark, H.L., Tunnell, D., 1985. Qualitative near-infrared reflectance analysis using

544   Mahalanobis distances. Anal. Chem. 57, 1449–1456.

545   https://doi.org/10.1021/ac00284a061

546 Nawar, S., Mouazen, A.M., 2017. Predictive performance of mobile vis-near infrared

547   spectroscopy for key soil properties at different geographical scales by using spiking and

548   data mining techniques. CATENA 151, 118–129.

549   https://doi.org/10.1016/j.catena.2016.12.014

550 Peng, X., Shi, T., Song, A., Chen, Y., Gao, W., 2014. Estimating soil organic carbon using

551   VIS/NIR spectroscopy with SVMR and SPA methods. Remote Sens. 6, 2699–2717.

552   https://doi.org/10.3390/rs6042699

553 Perga, M.-E., Frossard, V., Jenny, J.-P., Alric, B., Arnaud, F., Berthon, V., Black, J.L., Domaizon,

554   I., Giguet-Covex, C., Kirkham, A., Magny, M., Manca, M., Marchetto, A., Millet, L.,

555   Paillès, C., Pignol, C., Poulenard, J., Reyss, J.-L., Rimet, F., Sabatier, P., Savichtcheva, O.,

556   Sylvestre, F., Verneaux, V., 2015. High-resolution paleolimnology opens new

557   management perspectives for lakes adaptation to climate warming. Front. Ecol. Evol. 3,

558   72. https://doi.org/10.3389/fevo.2015.00072

559 Rosén, P., Vogel, H., Cunningham, L., Hahn, A., Hausmann, S., Pienitz, R., Zolitschka, B.,

560   Wagner, B., Persson, P., 2011. Universally Applicable Model for the Quantitative

561   Determination of Lake Sediment Composition Using Fourier Transform Infrared

562   Spectroscopy. Environ. Sci. Technol. 45, 8858–8865.

563 Tetko, I. V., Livingstone, D.J., Luik, A.I., 1995. Neural network studies. 1. Comparison of

564   overfitting and overtraining. J. Chem. Inf. Model. 35, 826–833.

565   https://doi.org/10.1021/ci00027a006

566 Van Exem, A., Debret, M., Copard, Y., Vannière, B., Sabatier, P., Marcotte, S., Laignel, B.,

567   Reyss, J.-L., Desmet, M., 2018. Hyperspectral core logging for fire reconstruction

568   studies. J. Paleolimnol. 59, 297–308. https://doi.org/10.1007/s10933-017-0009-5

569 Vidal, M., Amigo, J.M., 2012. Pre-processing of hyperspectral images. Essential steps before

570   image analysis. Chemom. Intell. Lab. Syst. 117, 138–148.

571   https://doi.org/10.1016/J.CHEMOLAB.2012.05.009

572 Viscarra Rossel, R.A., Behrens, T., 2010. Using data mining to model and interpret soil diffuse

573   reflectance spectra. Geoderma 158, 46–54.

574   https://doi.org/10.1016/j.geoderma.2009.12.025

575 Vohland, M., Ludwig, M., Thiele-Bruhn, S., Ludwig, B., 2014. Determination of soil properties

576   with visible to near- and mid-infrared spectroscopy: Effects of spectral variable

577   selection. Geoderma 223, 88–96. https://doi.org/10.1016/j.geoderma.2014.01.013

578 Wijewardane, N.K., Ge, Y., Wills, S., Loecke, T., 2016. Prediction of Soil Carbon in the

579   Conterminous United States: Visible and Near Infrared Reflectance Spectroscopy

580 Analysis of the Rapid Carbon Assessment Project. Soil Sci. Soc. Am. J. 80, 973–982.

581 https://doi.org/10.2136/sssaj2016.02.0052

582 Wold, S., Ruhe, A., Wold, H., Dunn, III, W.J., 1984. The Collinearity Problem in Linear

583 Regression. The Partial Least Squares (PLS) Approach to Generalized Inverses. SIAM J.

584 Sci. Stat. Comput. 5, 735–743. https://doi.org/10.1137/0905052

585 Zornoza, R., Guerrero, C., Mataix-Solera, J., Scow, K.M., Arcenegui, V., Mataix-Beneyto, J.,

586 2008. Near infrared spectroscopy for determination of various physical, chemical and

587 biochemical properties in Mediterranean soils. Soil Biol. Biochem. 40, 1923–1930.

588 https://doi.org/10.1016/j.soilbio.2008.04.003

589

590 **Tables**

591

592 *Table 1: Performance of complete and reduced PLSR models for the LOI550 prediction without removing water bands in blue*

593 *and after removing them in green.*

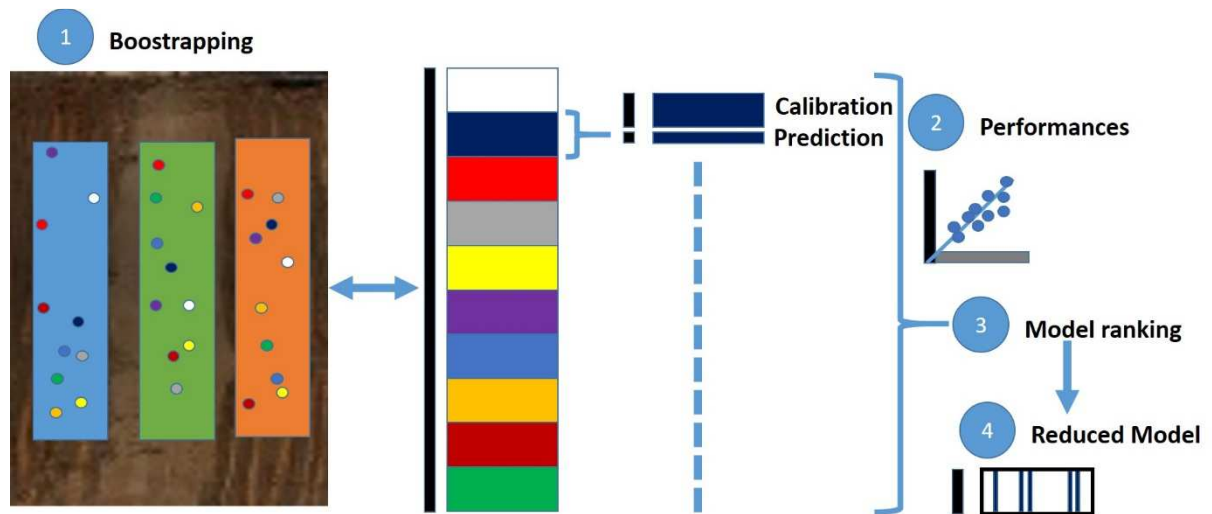| Wavelengths	Latent Variable	r calibration	r prediction	Model uncertainty (wt%)
121	8	0.99	0.80	1.40
21	7	0.96	0.88	1.20
75	7	0.99	0.92	1.02
27	**6**	**0.98**	**0.95**	**0.77**

594

595

Figure captions
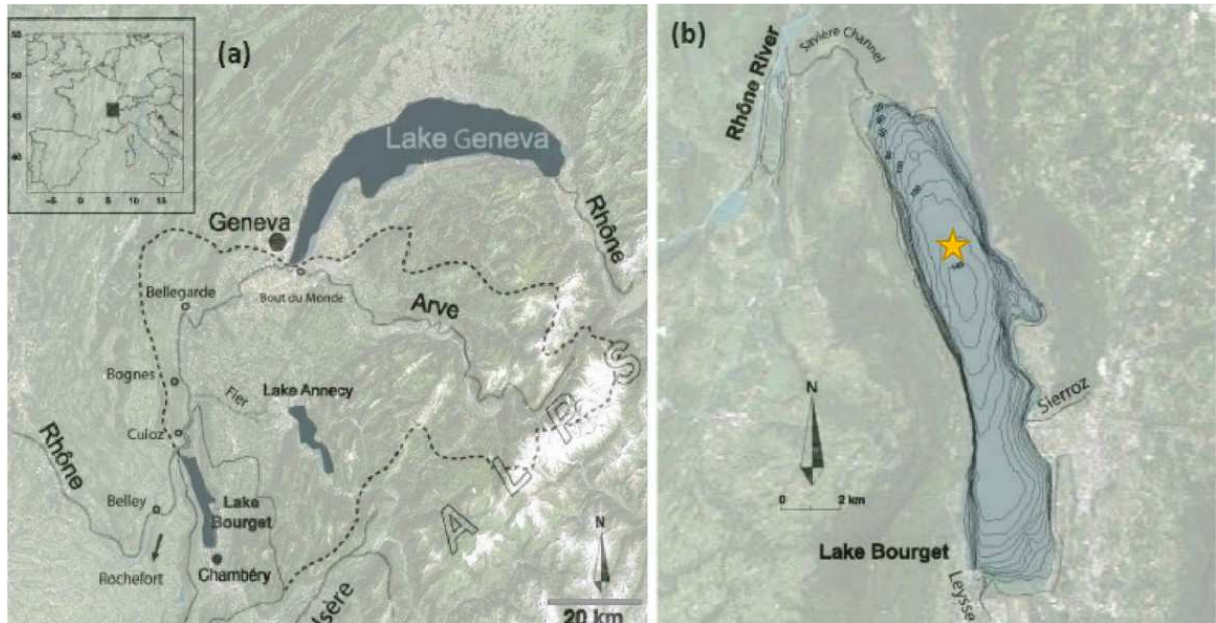
Figure 1: (a) Location and catchment area of Lake Bourget. (b) Bathymetry, tributaries and effluents of the lake.

Figure 2: The four principal steps followed to create a model: (1) dataset creations with bootstrapping in the sampling area that are associated with the corresponding LOI550 value, (2) create models, estimate performances and estimate the regression coefficients, (3) rank the models based on their performances, and (4) reduce the number of wavelengths with 10 optimal models and create the reduced model.
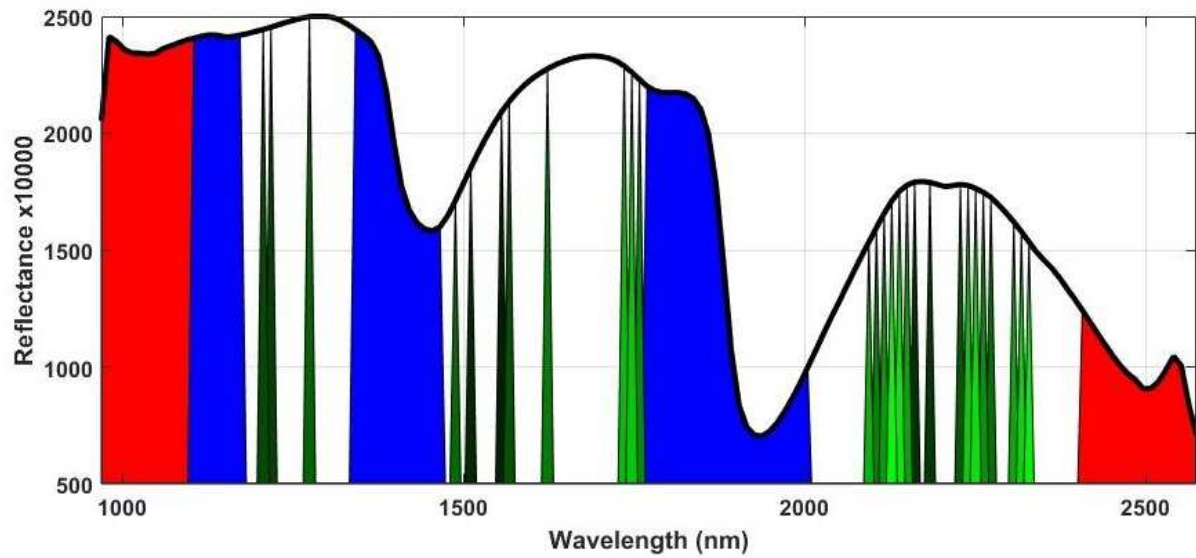
Figure 3: 27 most correlated wavelengths to LOI550 are highlighted with a green gradient (light green: most), the water bands are in blue, and the noise bands are in red on the mean spectrum in black.
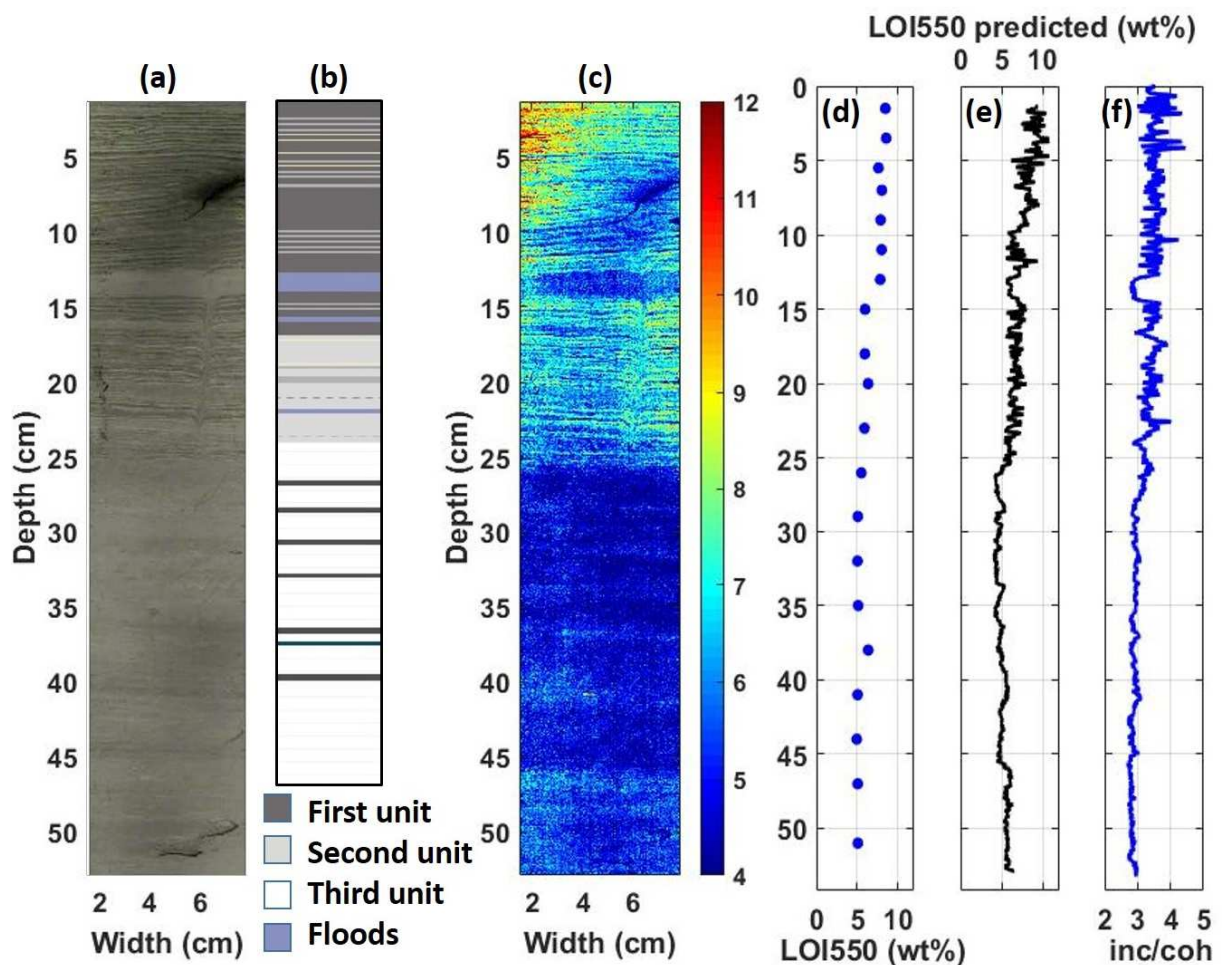
609   *Figure 4: Lake Bourget (a) RGB image, (b) lithology units, (c) LOI550 predicted concentration map with the reduce model, (d)*

610   *LOI550 reference values, (e) average LOI550 predicted values, and (f) inc/coh ratios.*
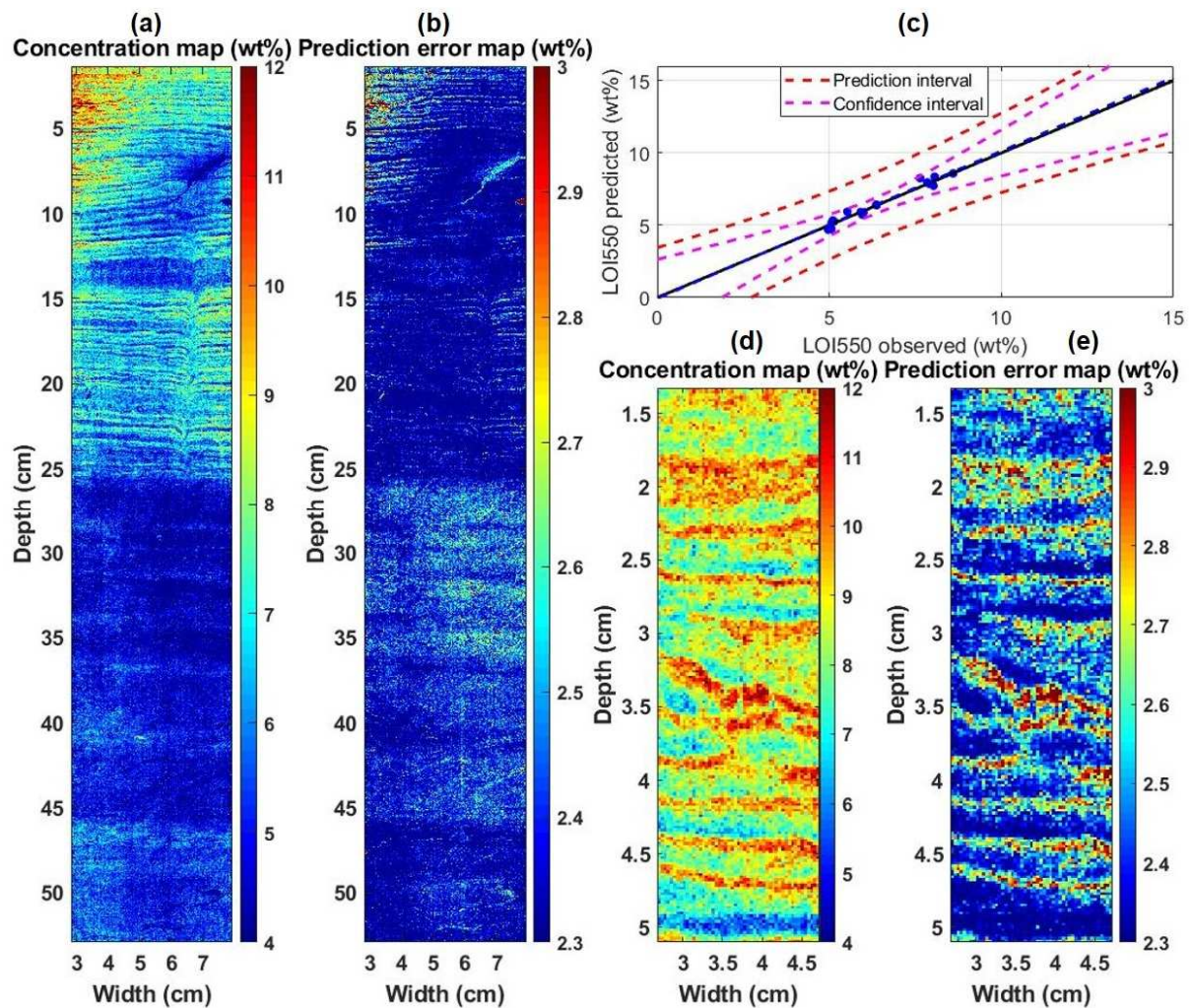
611

612   *Figure 5: (a) Concentration map of the core with its prediction error map (b). (c) Prediction and confidence intervals of the*

613   *LOI550 model. (d) Concentration map of a varved area and his prediction error map (e).*

614
615
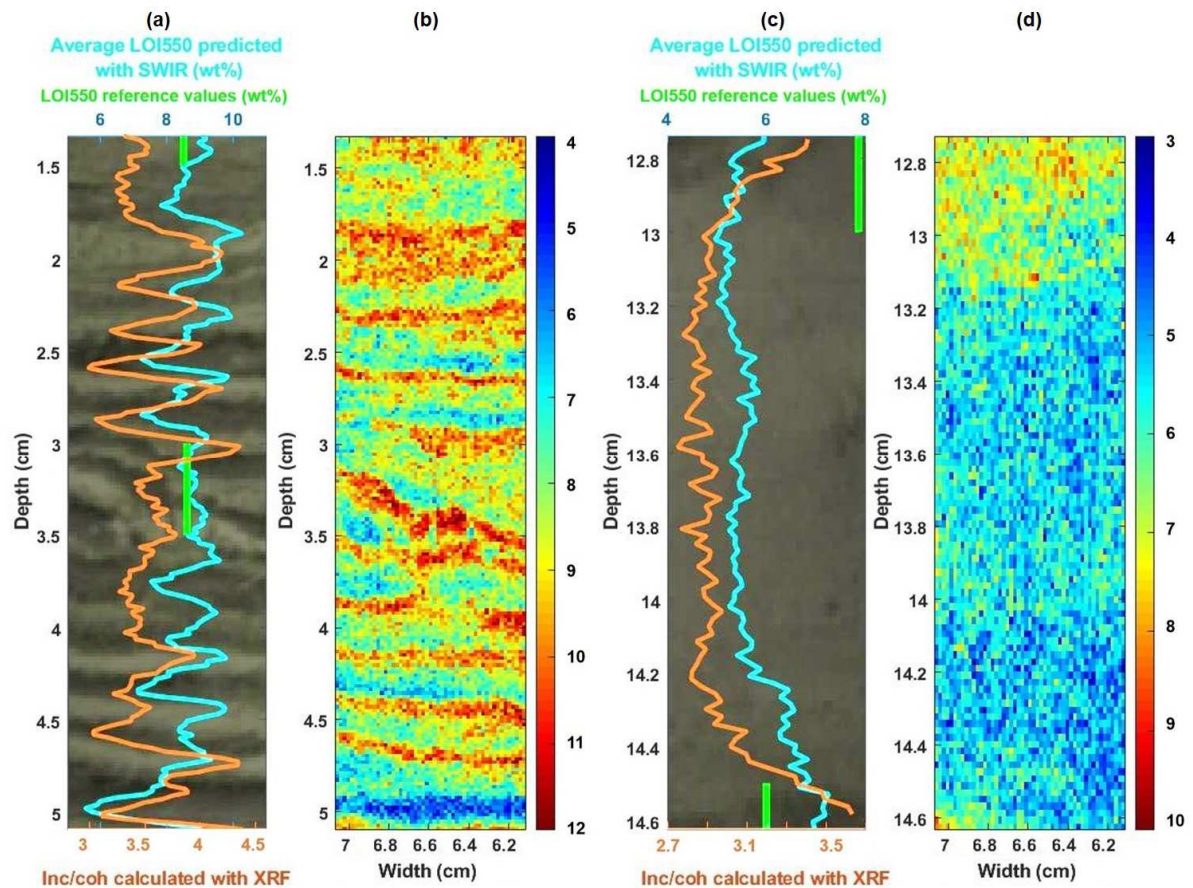
Figure 6: Zoom in for two areas on unit 1: varve (a-b) and flood (c-d). RGB image (a-c) with LOI550 reference values (green line) predicted by SWIR data (blue curve) and the inc/coh ratio (orange curve) as well as LOI550 concentration maps (b-d).